

# A statistical understanding of oxygen vacancies in distorted high-entropy oxides

Adam Potter<sup>1</sup>, Yifan Wang<sup>1</sup>, Dongjae Kong<sup>1</sup>, Yuzhe Li<sup>1</sup>, Jian Qin<sup>2</sup>, Xiaolin Zheng<sup>1,3,\*</sup>

<sup>1</sup>*Department of Mechanical Engineering, Stanford University, Stanford, CA, USA*

<sup>2</sup>*Department of Chemical Engineering, Stanford University, Stanford, CA, USA and*

<sup>3</sup>*Department of Energy Science and Engineering, Stanford University, Stanford, CA, USA\**

High entropy perovskite oxides (HEPOs) have emerged as a promising family of stable electrode materials for high-temperature water splitting. The concentration of oxygen vacancies in HEPOs significantly influences critical properties, such as the ionic conductivity and thermal expansion coefficient. However, predicting oxygen vacancy concentrations for the design of HEPOs with high-entropic A-sites remains challenging due to the complex arrangements of metal cations. Our experimental findings reveal that variations in A-site cation size constitute a crucial factor in affecting the oxygen vacancy concentration. High-throughput atomistic simulations using a machine-learned universal interatomic potential reveal that the lattice distortions from A-site size variations result in a broadened distribution of oxygen vacancy formation energies. Our theoretical analysis, grounded in statistical thermodynamics, provides formulations for the enthalpy and entropy of oxygen vacancy formation as functions of variance in oxygen bonding energy. Altogether, our results show mixing metal cations of varying sizes in the A-site creates statistical effects on the oxygen vacancy thermodynamics, resulting in a unique approach to tuning their concentrations for complex perovskite oxides.

Keywords: high-entropy perovskite oxide, oxygen vacancy, SOEC, oxygen electrode

## I. INTRODUCTION

Perovskite oxides ( $\text{ABO}_{3-\delta}$ ), such as LSCF ( $\text{La}_{0.6}\text{Sr}_{0.4}\text{Co}_{0.2}\text{Fe}_{0.8}\text{O}_{3-\delta}$ ), are widely utilized as anodes for high-temperature solid oxide electrolyzer cells (SOECs), which offer the potential for efficient hydrogen production using renewable energy and heat. However, the performance of SOECs is often limited by anode properties, including low oxygen ion conductivity and high thermal expansion [1]. The oxygen ion conductivity of perovskites relies on a high concentration of oxygen vacancies ( $\delta$ ) to enable efficient ion conduction via vacancy hopping [2]. The concentration of oxygen vacancies also affects other important properties, such as the thermal expansion coefficient, thermochemical stability, and electrical conductivity [3, 4]. As a result, understanding and careful control of oxygen vacancy behavior is critical for optimizing the performance of perovskite oxides in high-temperature SOECs.

Recently, high entropy perovskite oxides (HEPOs) ( $\text{ABO}_{3-\delta}$ ), with five or more cations with nearly equal molar amounts in either A- or B-site [5], have attracted great attention for SOECs as they theoretically could have good high-temperature chemical and structural stability due to the high mixing entropy [2]. In addition, high-entropy perovskites were shown to introduce bond distortion [6] and local ordering [7], which could potentially influence the formation of oxygen vacancies. It has been demonstrated that substituting metal cations can change the oxygen vacancy concentration [3, 8, 9]. However, exactly how the oxygen vacancy concentration in HEPOs varies with metal cation composition and tem-

perature remains elusive as the net energy needed to remove a lattice oxygen is significantly complicated by variations from different metal cations and configurational entropy.

Previous research on simple perovskites has provided valuable methodologies and insights for studying oxygen vacancy. For example, experimental studies vary concentrations of one or two metal cations systematically and measure oxygen vacancies using techniques, such as thermo-gravimetry analysis (TGA) [4, 10–14], Columbic titration [9, 15–17], X-ray photoelectron spectroscopy (XPS) [8], or iodometric titration [17]. Then, the vacancies' formation thermodynamics can be determined by applying concentration data to established defect models [3, 16]. Those studies consistently reveal the importance of the concentration of  $2+$  cations in the A-site ( $X_{2+}$ ) for forming high oxygen vacancy concentrations [12, 16]. However, experimentally sweeping every metal cation concentration is impractical for high-entropy materials with five or more dopants, and no such experimental studies have been reported in the literature.

In comparison, there are a few computational studies that aim to predict high-entropy doping effects on the oxygen vacancy concentration by calculating vacancy formation energies ( $E_v$ ). Density functional theory (DFT) studies calculated  $E_v$  for simple [11] and high-entropy oxides [7, 8, 13] and found cation substitutions could tune  $E_v$  as well as where vacancies preferred to form. An empirical study found such DFT-calculated  $E_v$  values could be predicted from the oxide's formation enthalpy, electronegativity, and band gap [18]. However, while it is possible to predict  $E_v$  for many high-entropy oxide compositions computationally, these  $E_v$  predictions have yet to consistently align with experimentally measured oxygen vacancy concentrations. A recent study by Park et al. [13] calculated  $E_v$  with DFT across many oxygen

\* Corresponding author: xlzheng@stanford.edu

sites for one HEPO and three simpler oxides and found all four had significant deviations in  $E_v$  depending on their cation neighbors. To address this variability, Park proposed  $E_v$  values exist in a distribution, noting the potential implications of the mean and variance on equilibrium vacancy concentration. Xu et al. [7] also used a statistical approach in their DFT study of complex perovskites to predict oxygen vacancy formation, finding that vacancies preferentially form near cobalt sites. Both studies suggest the statistics of  $E_v$  are key to understanding, predicting, and tuning oxygen vacancies and critical properties dependent on them. But the mechanisms of such statistical effects in high-entropy oxides across a range of compositions remain unexplored, both experimentally and computationally. This gap needs to be filled to provide principles or guiding models for the selection of cation dopants to tune oxygen vacancies in high-entropy materials.

In this work, we establish a combined experimental, computational, and theoretical workflow to study the effect of high-entropy mixed A-sites in perovskite oxides on the concentration of oxygen vacancies. Experimentally, we measured the oxygen vacancy concentration of 11 high-entropy (HE) and 3 low-entropy (LE) perovskites as a function of temperature using TGA, and found an enthalpy-entropy compensation relation where HE samples exhibit both lower enthalpy and entropy of oxygen vacancy formation. We found that the oxygen vacancy concentrations are directly affected by two primary variables: the conventional 2+ cation molar ratio in the A-site ( $X_{2+}$ ), and the newly identified A-site ionic radius variance ( $\sigma_A$ ). Computationally, we conducted high-throughput atomistic simulation with a machine-learned universal interatomic potential (MLUIP) to investigate the importance of  $\sigma_A$ . Our results show that greater variance among A-site cation radii ( $\sigma_A$ ) translates to higher variance in oxygen bonding energy ( $\sigma_{Ev}$ ), creating a broader distribution of vacancy formation energies in HE samples. Finally, using statistical thermodynamics, we derived expressions to explicitly show how this broadening in  $\sigma_{Ev}$  lowers both the enthalpy and configurational entropy per vacancy, consistent with the enthalpy-entropy compensation observed experimentally. Overall, the experimental, computational, and theoretical findings consistently highlight the significant impact of A-site metal cation size variations in affecting the oxygen vacancy concentration, providing a new approach to adjusting the oxygen vacancy concentrations for perovskite oxides.

## II. RESULTS

We study perovskites with LE (2-3 cations) and HE (5+ cations) A-sites taking the form  $A(Co_{0.2}Fe_{0.8})O_{3-\delta}$ , derived from LSCF, the state of the art for SOEC anodes [1, 19]. A-sites consist of Lanthanides and Alkaline earth metals and span a set of common compositional descrip-

tors, such as divalent metal cation concentration  $X_{2+}$  (Eq. 18), A-site cation size variance  $\sigma_A$  (Eq. 1), Goldschmidt tolerance factor  $t$  (Eq. 19), and mixing entropy  $\Delta S_{mix}$  (Eq. 20). We measure samples with both different and same A-site divalent (2+ cation) doping concentrations ( $X_{2+}$ ) to differentiate divalent doping from other A-site mixing effects.

### A. Experimental Estimation of Oxygen Vacancy Formation

All 14 perovskite oxides were synthesized using solution combustion synthesis followed by thermal annealing at 800°C and those oxide powders were further processed with high-speed ball-milling to break apart agglomerations (see Methods). Those oxides show a homogeneous distribution of elements, as illustrated by a representative sample HE-2 using scanning electron microscopy (SEM) paired with energy dispersive X-rays (EDX) (Figure S1a). The structure of all 14 oxides was characterized with X-ray diffraction (XRD) and found to match the same perovskite phase (orthorhombic  $Pnma$ ) (Figure S1b).

The change in oxygen vacancy concentration at temperature  $T$ ,  $\Delta\delta_T$ , was measured using TGA over 1-2 hours intervals starting from 500°C to 1000°C under ambient air. Stabilized mass readings suggest the vacancy formation reaction was in equilibrium (Figure S2). Initial vacancy concentrations in the experiment,  $\delta_0 = \delta(500^\circ C)$ , are expected to be small and were fit using nonlinear least squares (Table I) to a reaction model described below (Eq. 6), a typical approach for similar studies [4, 10, 12]. The oxygen vacancy concentration at temperature  $T$  is calculated from  $\delta_T = \delta_0 + \Delta\delta_T$  and shown in Figure 1a for all samples. The fitted  $\delta_0$  values range from 0.0005-0.014 and are indeed small compared to the measured concentration increase ranging from 0.035-0.13 seen in Figure 1a. As such, error in model-fit  $\delta_0$  values are likely to have marginal effects on the overall vacancy formation trends. The measured  $\delta(T)$  curve for LE-1 (equivalent to LSCF) in Figure 1a is in agreement with reported values for the similar composition ( $La_{0.6}Sr_{0.4}Fe$ ) $O_3$ :  $\delta=0.044$  vs 0.035 in [20] at 900°C.

Upon close examination of Figure 1a, it can be seen that the HE samples (solid lines) tend to exhibit more oxygen vacancies than LE samples (dashed lines), particularly at temperatures  $\leq 900^\circ C$ . Furthermore, the curves of the HE samples are quasilinear, but the LE samples show more exponential growth of oxygen vacancy concentration with temperature. Even among HE samples, HE-3 and HE-4 have steeper curves than HE-7 or HE-5. Figure 1b shows the oxygen vacancy concentration at 800°C as a function of the mole fraction of 2+ cations in the A-site ( $X_{2+}$ ), and clearly, larger values of  $X_{2+}$  lead to more vacancies in general for LE and HE samples. This is because  $X_{2+}$  is directly tied to the formation of oxygen vacancies as explained in Section II B. Despite the important role of  $X_{2+}$ , there are still large

Label	A-Site Composition	$X_{2+}$	$t$	$\sigma_A$ (%)	$\Delta S_{mix}$ (J/mol-K)	$\Delta H^f$ (kJ/mol)	$\Delta S^f$ (J/mol-K)	$\delta_0$ ( $10^{-3}$ )
LE-1	La <sub>0.6</sub> Sr <sub>0.4</sub> (LSCF)	0.40	0.978	2.82	5.60	90 $\pm$ 8	56 $\pm$ 7	0.79 $\pm$ 0.4
LE-2	La <sub>0.6</sub> Sr <sub>0.2</sub> Ca <sub>0.2</sub>	0.40	0.971	2.54	7.90	92 $\pm$ 8	60 $\pm$ 8	0.83 $\pm$ 0.4
LE-3	La <sub>0.7</sub> Ca <sub>0.3</sub>	0.30	0.965	0.68	5.08	77 $\pm$ 4	41 $\pm$ 3	0.55 $\pm$ 0.1
HE-1	La <sub>0.17</sub> Sr <sub>0.17</sub> Ca <sub>0.17</sub> Ba <sub>0.17</sub> Nd <sub>0.17</sub> Sm <sub>0.17</sub>	0.50	0.973	8.90	14.90	54 $\pm$ 7	33 $\pm$ 5	18 $\pm$ 9
HE-2	La <sub>0.2</sub> Sr <sub>0.2</sub> Ca <sub>0.2</sub> Nd <sub>0.2</sub> Y <sub>0.2</sub>	0.40	0.957	5.10	13.38	72 $\pm$ 4	57 $\pm$ 3	11 $\pm$ 3
HE-3	La <sub>0.2</sub> Sr <sub>0.2</sub> Ca <sub>0.2</sub> Nd <sub>0.2</sub> Sm <sub>0.2</sub>	0.40	0.957	5.10	13.38	71 $\pm$ 2	51 $\pm$ 2	7.6 $\pm$ 1
HE-4	La <sub>0.2</sub> Sr <sub>0.2</sub> Ca <sub>0.2</sub> Gd <sub>0.2</sub> Sm <sub>0.2</sub>	0.40	0.957	5.22	13.38	71 $\pm$ 2	52 $\pm$ 2	8.6 $\pm$ 1
HE-5	La <sub>0.2</sub> Sr <sub>0.2</sub> Ba <sub>0.2</sub> Gd <sub>0.2</sub> Nd <sub>0.2</sub>	0.40	0.978	9.05	13.38	52 $\pm$ 3	33 $\pm$ 2	14 $\pm$ 3
HE-6	La <sub>0.4</sub> Sr <sub>0.2</sub> Ba <sub>0.1</sub> Ca <sub>0.1</sub> Nd <sub>0.2</sub>	0.40	0.975	6.77	12.22	59 $\pm$ 1	35 $\pm$ 1	6.8 $\pm$ 0.3
HE-7	La <sub>0.2</sub> Ba <sub>0.1</sub> Ca <sub>0.3</sub> Nd <sub>0.2</sub> Y <sub>0.2</sub>	0.40	0.960	7.46	12.99	49 $\pm$ 5	26 $\pm$ 4	10 $\pm$ 4
HE-8	La <sub>0.17</sub> Sr <sub>0.17</sub> Ca <sub>0.17</sub> Gd <sub>0.17</sub> Nd <sub>0.17</sub> Sm <sub>0.17</sub>	0.33	0.953	5.10	14.90	72 $\pm$ 3	53 $\pm$ 3	5.2 $\pm$ 1
HE-9	La <sub>0.14</sub> Sr <sub>0.14</sub> Ca <sub>0.14</sub> Gd <sub>0.14</sub> Nd <sub>0.14</sub> Sm <sub>0.14</sub> Y <sub>0.14</sub>	0.29	0.950	5.12	16.18	73 $\pm$ 8	53 $\pm$ 7	3.3 $\pm$ 2
HE-10	La <sub>0.2</sub> Sr <sub>0.2</sub> Gd <sub>0.2</sub> Sm <sub>0.2</sub> Y <sub>0.2</sub>	0.20	0.950	5.80	13.38	74 $\pm$ 11	53 $\pm$ 10	1.6 $\pm$ 1
HE-11	La <sub>0.17</sub> Sr <sub>0.17</sub> Gd <sub>0.17</sub> Nd <sub>0.17</sub> Sm <sub>0.17</sub> Y <sub>0.17</sub>	0.17	0.948	5.46	14.90	72 $\pm$ 5	51 $\pm$ 4	1.2 $\pm$ 0.4

TABLE I. Low entropy (LE) and high entropy (HE) A-site compositions with B-Site (Co<sub>0.2</sub>Fe<sub>0.8</sub>) described with pre-calculated values: divalent mole fraction ( $X_{2+}$ ), tolerance factor ( $t$ ), size variance ( $\sigma_A$ ), and mixing entropy ( $\Delta S_{mix}$ ). Experimental formation enthalpies ( $\Delta H^f$ ), entropies ( $\Delta S^f$ ), initial vacancies at 500°C ( $\delta_0$ ) and uncertainties fit from TGA data with Eq.6.

unexplained variations in the concentration of oxygen vacancy between samples for the same  $X_{2+}=0.4$ , indicating that other factors also play an important role. Figure 1c plots the curvature of Figure 1a (in units 1/°C) against the A-site size variance  $\sigma_A$ . HE samples have consistently smaller curvatures and thus more linear growth of oxygen vacancies.  $\sigma_A$  is given by Eq. 1 in percent where  $r_{A,i}$  is the ionic radius of the  $i$ th A-site element out of  $N$  elements and  $\hat{r}_A$  is the average radius.

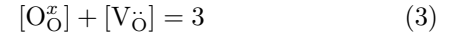
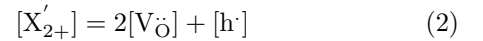
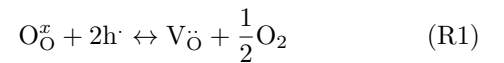
$$\sigma_A = 100 \cdot \frac{\sqrt{\sum_i^N (r_{A,i} - \hat{r}_A)^2}}{\sum_i^N r_{A,i}} \quad (1)$$

The importance of  $X_{2+}$  is well known in the literature and will be discussed in the context of defect reaction thermodynamics in the following section. In comparison, the importance of  $\sigma_A$  in oxygen vacancy thermodynamics is yet to be explored and will be the subject for the remainder of this paper.

## B. Determining Oxygen Vacancy Formation Thermodynamics

This section aims to determine the  $\Delta G^f$ ,  $\Delta H^f$ , and  $\Delta S^f$  values for the oxygen formation reaction (R1) for both the LE and HE samples. In reaction R1,  $O^x$  is lattice oxygen,  $h^\cdot$  are holes, and  $V_{\ddot{O}}$  are oxygen vacancies in Kroger-Vink notation. When the A-site of a perovskite is doped with a 2+ cation ( $X_{2+}$ ), its negative charge relative to other 3+ cations will be compensated by forming either a B-site hole ( $h^\cdot$ ) or half of an oxygen vacancy ( $V_{\ddot{O}}$ ) to maintain charge neutrality as expressed by Eq.2. The holes can be thought of as 4+ oxidation states of B-site cations (Fe<sup>+</sup> or Co<sup>+</sup>) with a net positive defect charge relative to the typical 3+ state, as the 2+ oxidation state of B-site elements (Fe<sup>+</sup>, Co<sup>+</sup>) has negligible concentrations in oxidizing conditions [10, 16]. This

relation assumes the following: 1) 2+ A-site doping is the dominant form of hole generation (i.e., the intrinsic charge carrier concentration is negligible); 2) only the B-site cations change oxidation states during the oxygen vacancy formation; and 3) holes are not differentiated by B-site element [16, 20, 21]. Moreover, as a perovskite unit cell has three oxygen sites, the sum of vacancies  $V_{\ddot{O}}$  and occupied sites  $O_O^x$  must equal three (Eq.3).



The equilibrium constant,  $K_{p,ox}$  for the oxygen formation reaction (R1) can be expressed as Eq. 4 considering the concentration relations in Eqs. 2-3 and assuming a reference oxygen partial pressure ( $pO_2^0$ ) of 1 bar.  $K_{p,ox}$  is now solely a function of  $X_{2+}$ ,  $pO_2$ , and  $\delta_T$  (Eq. 4) which are known or measured with TGA (Figure 1). Similar or identical expressions for the oxygen vacancy equilibrium constant have been used in previous studies [4, 10, 12, 14]. The explicit relation of oxygen vacancies,  $\delta_T$ , on the concentration of  $X_{2+}$  in this expression is consistent with that seen in Figure 1b.

$$K_{p,ox}(T) = \frac{[V_{\ddot{O}}] \left[ \frac{pO_2}{pO_2^0} \right]^{1/2}}{[O_O^x][h^\cdot]^2} = \frac{\delta_T \sqrt{pO_2}}{(3 - \delta(T))([X_{2+}] - 2\delta_T)^2} \quad (4)$$

This equilibrium constant can also be expressed as a function of the Gibbs of formation  $\Delta G^f$ , or equivalently enthalpy of formation  $\Delta H^f$  and entropy of formation  $\Delta S^f$  of oxygen vacancy, the specific gas constant  $R$ , and

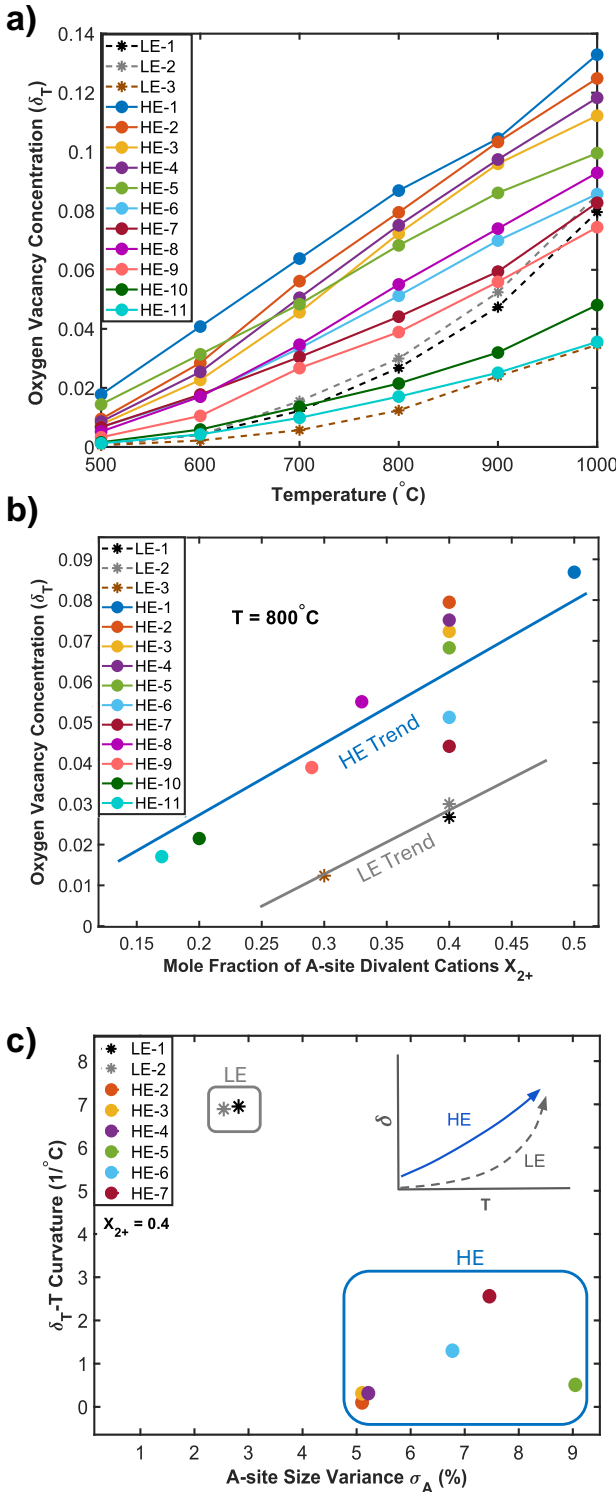


FIG. 1. (a) Experimental oxygen vacancy concentration  $\delta_T$  as a function of temperature from TGA (b)  $\delta_{800^\circ\text{C}}$  as a function of  $X_{2+}$  (c) curvature of  $\delta_T$ -T curves in Figure 1a as a function  $\sigma_A$  for samples with  $X_{2+}=0.4$

temperature  $T$  (Eq. 5). The combination of Eqs. 4, and

5 result in Eq. 6 below.

$$K_{\text{p,ox}}(T) = e^{-\frac{\Delta G^f}{RT}} = e^{\frac{\Delta S^f}{R} - \frac{\Delta H^f}{RT}} \quad (5)$$

$$\frac{\Delta S^f}{R} - \frac{\Delta H^f}{RT} = \ln \left[ \frac{(\delta_0 + \Delta \delta_T) \sqrt{pO_2}}{(3 - (\delta_0 + \Delta \delta_T))([X_{2+}] - 2(\delta_0 + \Delta \delta_T))^2} \right] \quad (6)$$

Now, the  $\delta_T$  curves measured by TGA for all 14 samples (Figure 2a) can be fit to Eq. 6 using nonlinear least squares to extract  $\Delta H^f$ ,  $\Delta S^f$ , and  $\delta_0$  ( $R^2 > 0.99$  for all samples) and the values are reported in Table I. The fitted values of  $\Delta H^f$  and  $\Delta S^f$  for LE-1 are very similar to previously reported values for the similar oxide ( $\text{La}_{0.6}\text{Sr}_{0.4}\text{FeO}_3$ ): 90 kJ/mol vs 95 kJ/mol [20] and 90 kJ/mol [21] for  $\Delta H^f$  and 56 J/mol-K vs 54 J/mol-K [20] and 58 J/mol-K [21] for  $\Delta S^f$ , validating the methodology.

### C. Differences in Vacancy Formation Free Energy for HE and LE Samples

This section aims to understand differences in  $\Delta G^f(T)$  between HE and LE samples that lead to the oxygen vacancy concentration differences at various temperatures. The Van't Hoff diagram (Figure 2a) shows  $\ln K_{\text{p,ox}}$  (or  $-\Delta G^f/RT$ ) vs  $1/T$  (Eq. 5) exclusively for samples with same  $X_{2+} = 0.4$ .  $\Delta S^f$  and  $\Delta H^f$  and are the intercept and negative of the slope respectively. LE and HE samples show clearly different trends; HE samples exhibit a larger  $K_{\text{p,ox}}$  (smaller  $\Delta G^f$ ) at lower temperatures indicating more oxygen vacancies. With increasing temperature, the  $K_{\text{p,ox}}$  of HE samples increases slower than that of LE samples due to their smaller  $\Delta H^f$ . This is equivalent to the oxygen vacancy concentration of HE samples increasing linearly, instead of exponentially, with temperature (Figure 1a and 1c).

We conducted a correlation study between the measured  $\Delta H^f$  and  $\Delta S^f$  (Table I) and four compositional descriptors ( $X_{2+}$ ,  $t$ ,  $\sigma_A$ ,  $\Delta S_{\text{mix}}$ ) across  $n=14$  samples (see details in Methods) shown in Figure 2b. Such a correlation study has not been reported previously. First, the cross-correlation of the four compositional descriptors is limited, suggesting the chosen sample compositions effectively span a four-dimensional A-site design space. In addition,  $\Delta H^f$  and  $\Delta S^f$  are not strongly correlated with  $X_{2+}$ , indicating the dependence seen in Figure 1b is encapsulated by the inclusion of  $X_{2+}$  in the equilibrium constant (Eq. 4).  $\Delta H^f$  and  $\Delta S^f$  show moderate correlations with  $\Delta S_{\text{mix}}$  and tolerance factor  $t$ , but strong correlation with the A-site size variance  $\sigma_A$ .

When our experimentally measured  $\Delta H^f$  and  $\Delta S^f$  (isolating  $X_{2+} = 0.4$ ) are plotted against  $\sigma_A$  (Figures 2c and 2d), their clear correlations can be fit with empirical relations included in the plots. When we added

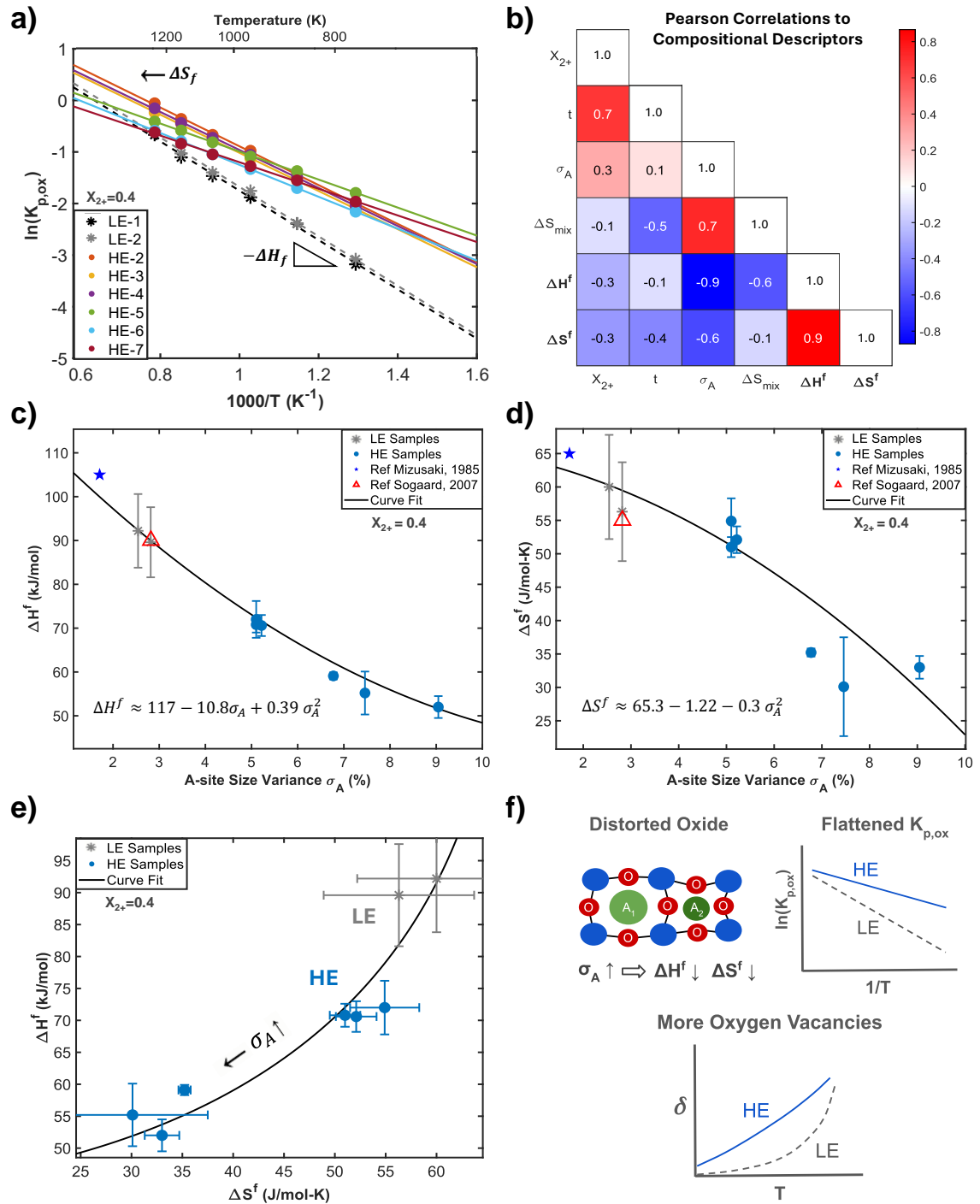


FIG. 2. (a) Van't Hoff diagram showing the oxygen vacancy formation equilibrium constant  $K_{p,\text{ox}}$  for samples with  $X_{2+} = 0.4$  b) Pearson correlation matrix linking  $\Delta H^f$  and  $\Delta S^f$  to four compositional descriptors c) formation enthalpy  $\Delta H^f$  as a function of  $\sigma_A$  and (d) formation entropy  $\Delta S^f$  as a function of  $\sigma_A$  both with values from two references (e) correlation between  $\Delta H^f$  and  $\Delta S^f$  roughly scaling with  $\sigma_A$  (f) distorted oxides with high  $\sigma_A$  exhibit a larger, flatter  $K_{p,\text{ox}}$  leading to higher oxygen vacancy concentrations that grow linearly with temperature

$\Delta H^f$  and  $\Delta S^f$  values reported by [14] and [21] for variants of LE-1, they nicely follow the trends. The  $\Delta H^f$  relationship with  $\sigma_A$  in Figure 2c ( $R^2=0.95$ ) and  $\Delta S^f$

relationship in Figure 2d ( $R^2=0.83$ ) are quasilinear or quadratic. Together, we can observe a positive correlation between  $\Delta H^f$  and  $\Delta S^f$  in Figure 2e. This empir-

ical correlation between  $\Delta H^f$  and  $\Delta S^f$  within a family of materials, known as enthalpy-entropy compensation, has been documented for reactions in other systems, although there is no agreement on the underlying mechanism [22, 23]. Suggested mechanisms include solvent interactions, hidden reaction intermediates [22], and numerical artifacts from data fitting [24], the last of which should not apply as our  $\Delta G^f$  values are distinct between LE and HE samples (Fig 2a).

A proposed relationship between oxygen vacancies and the A-site size variations is summarized in Figure 2f. Introducing mismatches in the A-site cation size induces distortion in the lattice [6] and strains oxygen bonds [13] which reduces  $\Delta H^f$  and  $\Delta S^f$ . In short, a larger  $\sigma_A$  (e.g. HE samples) leads to a flatter  $\Delta G^f$ , and hence a slower increase in oxygen vacancy with temperature (Figure 1a).

#### D. Quantifying the Impact of $\sigma_A$ on Vacancy Formation Energies using a Deep Learning Potential

The formation enthalpy  $\Delta H^f$  of oxygen vacancies is a function of the energy to create an oxygen vacancy,  $E_v$ , which can be calculated with atomistic simulations.

$$\Delta H^f = f(E_v) \quad (7)$$

A unique aspect of disordered high entropy materials is that the vacancy energies  $E_v$  vary across lattice sites, so we need to estimate  $\Delta H^f$  and  $\Delta S^f$  statistically using a distribution of vacancy energies  $g(E_v)$ . This is accomplished by sampling hundreds of oxygen sites in an atomistic simulation using a machine learning universal interatomic potential (MLUIP) provided by Matlantis [25]. To control for contributions from divalent doping, only the eight materials in Table I with  $X_{2+} = 0.4$  are considered. All materials are modeled with an orthorhombic *Pnma* perovskite phase which fits well with XRD data (Figure S1). Large randomly populated perovskite supercells are generated in the Atomic Simulation Environment [26] to represent LE and HE samples (Figure S3). The resulting simulation cell contains 1280 atoms (256 perovskite unit cells), large enough that even the sparsest A-site element is represented within 2% of its stated mole fraction.

##### 1. Structural Simulations and $\sigma_A$ and Vacancy Energy

Vacancy energy  $E_v$  will be related to the B-site oxygen bonding as it is typically stronger than A-site oxygen bonding and dominates the bonding energy in perovskites [27]. Intuitively, variations in A-site size will cause variations in B-site bonding (Figure 3a) [27]. To quantify this, we first find the energy-minimized structures of the initial supercells of various HE and LE samples with no oxygen vacancies. After energy minimization of each supercell, we record the bond lengths and

bond angles of B-O bonds for all 768 oxygen atoms (see Methods). As shown in Figure 3b, a large variance in A-site cation size  $\sigma_A$  leads to higher root mean squared deviations (RMSD) for both the B-O bond lengths and the B-O-B bond angles. This suggests that large  $\sigma_A$  leads to a broader distribution of B-site oxygen bonding geometries, hence a broader distribution of energy to create an oxygen vacancy.

The oxygen vacancy formation energy  $E_v$  is calculated using Eq. 8, where  $E_{\text{bulk}}$  and  $E_{\text{defect}}$  are the total energy of a relaxed supercell before and after removing one oxygen atom, and  $E_{O_2}$  (-9.52 eV) is the energy from forming gaseous oxygen estimated from the tabulated elemental phase reference of oxygen [28]. It should be noted that our calculated vacancy formation energy values range from 0.15 to 1.4 eV, much larger than the mean average error of 0.03 eV relative to DFT the MLUIP reports for disordered systems [25], so MLUIP error is likely relatively small in our calculations.

$$E_v = E_{\text{defect}} - E_{\text{bulk}} + \frac{1}{2}E_{O_2} \quad (8)$$

Calculated  $E_v$  values for HE samples are higher variance compared to LE samples (Table II).  $g(E_v)$  represents the probability distribution of a given oxygen site having vacancy formation energy  $E_v$ . Curves for  $g(E_v)$  in Figure 2c are estimated by sampling  $E_v$  for all oxygen sites in the supercell and smoothing the distribution using a kernel density estimation with bandwidth 0.03eV. Figure 3c shows that the means  $\hat{E}_v$  for the two HE and one LE samples are comparable, but the two HE samples have a higher variance, as we expected from Figure 3b. The longer tail of the distribution where  $E_v < 0.4$ eV suggests that more oxygen vacancies will be generated at lower temperatures for HE samples. Park *et al.* suggested a similar effect of high-variance  $g(E_v)$  distributions in their DFT study of disordered perovskites, although experimental verification of this model was inconclusive [13]. Notably, the average sampled vacancy energy  $\hat{E}_v$  across all HE samples was comparable the average for LE samples (0.68 vs 0.69 eV) while their average vacancy energy standard deviations  $\sigma_{E_v}$  diverged significantly (0.14 vs 0.22 eV) suggesting  $E_v$  variance is key to differentiating LE and HE vacancy behavior (Table II). Next, we will use statistical thermodynamics to understand how the broadening of  $g(E_v)$  in HE samples leads to observed differences in  $\Delta H^f$  and  $\Delta S^f$ .

#### E. Oxygen Vacancy Energy and Statistical Thermodynamics

Oxygen vacancies can be modeled as the exchange of lattice oxygen with an external reservoir at a fixed temperature, described by the grand canonical ensemble. Each site either binds to an atom or not, so they can be treated as ideal Fermions following Fermi-Dirac

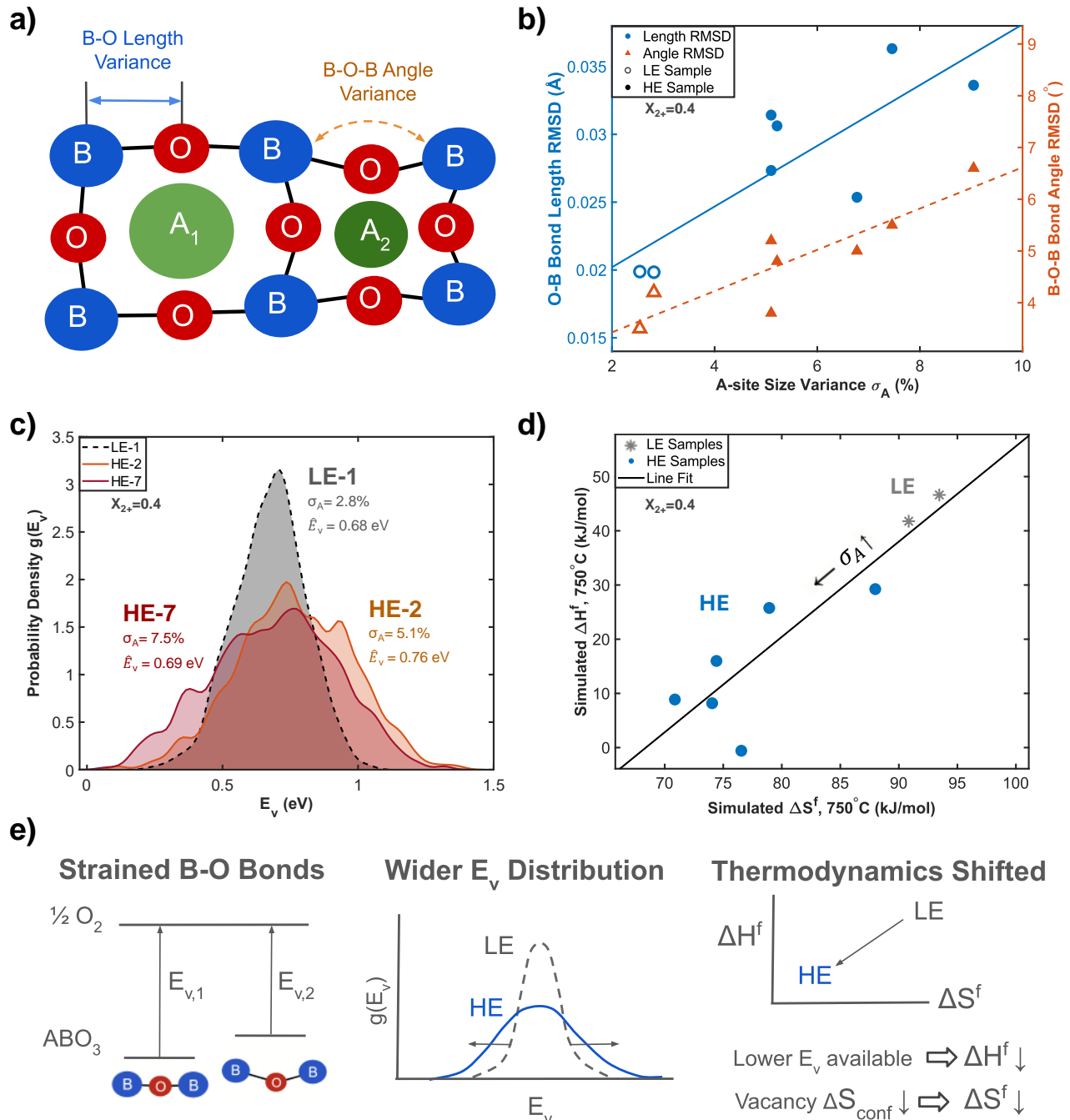


FIG. 3. (a) Variance in the length and angle of oxygen bonded to B-site cations (b) root mean squared deviation in bond length and angle as a function of A-site size variance  $\sigma_A$  (c) simulation sampled distributions of vacancy formation energies  $g(E_v)$  for select LE and HE compositions (d) correlation between  $\Delta H^f$  and  $\Delta S^f$  predicted from simulated  $g(E_v)$  with Eqs. 13-14 (e) A-site size mismatch can strain B-O bonds increasing variance in  $E_v$  resulting in both lower  $\Delta H^f$  and  $\Delta S^f$

statistics. In this ensemble, the probability of site  $i$  being vacant,  $p_{v,i}$ , is given by Eq. 9 where  $\epsilon_i$  is the free energy of an oxygen vacancy on site  $i$ ,  $\mu_v$  is the chemical potential of the oxygen vacancies in the system, and  $k_B$  is the Boltzmann constant. The oxygen vacancy fraction  $x$ , equivalent to the vacancy concentration  $\delta$  over three, is

the probability of vacancy averaged over  $N$  oxygen sites (Eq. 10).

$$p_{v,i} = \frac{1}{1 + e^{(\epsilon_i - \mu_v)/k_B T}} \quad (9)$$

Label	$\hat{E}_v$ (eV)	Avg $\hat{E}_v$ (eV)	$\sigma_{Ev}$ (eV)	Avg $\sigma_{Ev}$ (eV)
LE-1	0.68	0.68	0.13	0.14
LE-2	0.68		0.15	
HE-2	0.76	0.69	0.21	0.22
HE-3	0.76		0.24	
HE-4	0.76		0.23	
HE-5	0.54		0.22	
HE-6	0.61		0.17	
HE-7	0.69		0.23	

TABLE II. Simulated oxygen vacancy energy distributions,  $g(E_v)$ , with mean  $\hat{E}_v$  and standard deviation  $\sigma_{Ev}$  sampled from 768 oxygen sites for compositions with  $X_{2+} = 0.4$  including average values over LE and HE samples

$$x := \frac{\delta}{3} = \frac{1}{N} \sum_{i=1}^N p_{v,i} \quad (10)$$

This vacancy probability  $p_{v,i}$  is key to the statistical calculation of  $\Delta H^f$  and  $\Delta S^f$ . Finding  $p_{v,i}$  (Eq. 9) depends on the vacancy free energy at each site  $\epsilon_i$ , which we will treat as a distribution with average free energy  $\hat{\epsilon}$  and variance  $\sigma_\epsilon^2$  (Eq. 11) due to small perturbations from the mean.

$$\sigma_\epsilon^2 = \frac{1}{N} \sum_{i=1}^N (\epsilon_i - \hat{\epsilon})^2 \quad (11)$$

Given this problem setup, the objective of this derivation is to find the first-order effects of energy perturbations due to variance  $\sigma_\epsilon^2$  on predicted values of  $\Delta H^f$  and  $\Delta S^f$ . The first-order effects are derived in detail in the Supplemental. In short, by expanding around first order terms of  $\sigma_\epsilon^2$ , we inverted Eqs. 9-10 to arrive at an expression for oxygen vacancy chemical potential  $\mu_v$  as a function of vacancy fraction  $x$  and  $\sigma_\epsilon^2$  (Eq. 12). Eq. 12 conforms to that for the regular solution theory [29]: the correction to the ideal mixing given by the rightmost term, of scale  $\sigma_\epsilon^2/(k_B T)$ , is the contribution from the interactions between vacant sites and occupied sites. When energy broadening  $\sigma_\epsilon$  is sufficiently large, this additional term can be a substantial correction which has not been reported before and can be prominent for high entropy materials.

$$\mu_v = \hat{\epsilon} + k_B T \left[ \ln \left( \frac{x}{1-x} \right) + \left( x - \frac{1}{2} \right) \frac{\sigma_\epsilon^2}{(k_B T)^2} \right] \quad (12)$$

In equilibrium, the chemical potential of lattice oxygen equals that of oxygen in the environment. Constitutive assumptions outlined in the Supplemental connect free energy of vacancies  $\epsilon_i$  and vacancy chemical potential  $\mu_v$  to vacancy energy  $E_v$  and gaseous oxygen formation entropy  $S_{O_2}$  (a tabulated value). We assume that variations in free energy is primarily due to variations in the vacancy energy, that is,  $\sigma_\epsilon = \text{Var}[E_v] = \sigma_{Ev}$ . Equating chemical potentials and collecting terms results in expressions for

$\Delta H^f$  and  $\Delta S^f$  as they are used in the law of mass action (Eqs. 4-5). This results in Eqs. 13 and 14 which are valid for a small  $\sigma_{Ev}$  and small vacancy fractions ( $x$ ). Full details, including expressions valid for larger vacancy fractions ( $x$ ), can be found in the Supplemental.

The first derived expression, Eq. 13, predicts oxygen vacancy formation enthalpy  $\Delta H^f$  including the first-order effects from broadening  $g(E_v)$ . This expression is a departure from the assumption of uniform vacancies where  $\Delta H^f = \hat{E}_v$  [8, 11, 13, 30] and is relevant for disordered or high-entropy materials where  $\sigma_{Ev} > 0$ . This correction can be large: for  $\sigma_{Ev} = 0.2\text{eV}$ , our typical value for HE materials, this correction reduces  $\Delta H^f$  by 45 kJ/mol at 1000K. At the limit of small vacancy concentrations, broadening  $g(E_v)$  will always lower  $\Delta H^f$ . This is an intuitive result because  $g(E_v)$  will have a larger tail in the low  $E_v$  region; more low  $E_v$  oxygen sites will be available for vacancies. This is consistent with Park's numerical results that shifting  $\sigma_{Ev}$  can shift the equilibrium oxygen vacancy concentration [13]. The analytical expression in Eq. 13 gives an interpretable starting point for researchers to harness disorder-induced energy broadening to tune defect thermodynamics.

$$\Delta H^f \approx \hat{E}_v - \frac{\sigma_{Ev}^2}{k_B T} \quad (13)$$

The second derived expression, Eq. 14, similarly predicts the effects of oxygen vacancy energy broadening on  $\Delta S^f$ . This is a departure from the common assumption  $\Delta S^f = \frac{1}{2} S_{O_2}$  for oxygen vacancies [7, 11, 13]. At low vacancy concentrations, broadening  $g(E_v)$  always reduces the effective change in entropy. This is because introducing oxygen sites that favor vacancies (low  $E_v$ ) increases the likelihood of configurations where those sites are vacant, lowering the configurational entropy. Skewing  $p_{v,i}$  away from the uniform case where  $p_{v,i} = \hat{p}_v$  always lowers configurational entropy. In short, having preferred sites for oxygen vacancies results in less configurational entropy, an effect propagated to a smaller  $\Delta S^f$ .

$$\Delta S^f \approx \frac{1}{2} S_{O_2} - \frac{\sigma_{Ev}^2}{2k_B T^2} \quad (14)$$

We now have a theoretical basis for explaining the experimentally observed enthalpy-entropy correlation (compensation mechanism) for oxygen vacancies (Figure 2e). Eqs. 13 and 14, found by approximating the first-order effects of  $\sigma_{Ev}$  from first-principles, correctly predict HE samples with higher  $\sigma_{Ev}$  will exhibit lower  $\Delta H^f$  and  $\Delta S^f$ . In fact, Eqs. 13 and 14 can be combined in Eq. 15 to predict a  $\Delta H^f - \Delta S^f$  scaling relation when  $\hat{E}_v$  and  $S_{O_2}$  are constant.

$$\Delta H^f = (2T) \Delta S^f + (\hat{E}_v - T S_{O_2}) \quad (15)$$

Eq. 15 suggests the scaling between  $\Delta H^f$  vs  $\Delta S^f$  from perturbing  $\sigma_{Ev}$  is approximately  $2T$ . This prediction can be compared with our experimental results because simulated  $\hat{E}_v$  values are comparable across LE and HE samples (Table II). The slope of the line of best fit in Figure

2e, known as the compensation or isoequilibrium temperature [23], is found to be 1120K, a comparable order of magnitude to the predicted slope of  $2T$  (1500-2500K).

The scaling relation between  $\Delta H^f$  and  $\Delta S^f$  has opposing effects on the Gibb's of formation  $\Delta G^f$  with the enthalpy term winning. For a small vacancy fraction  $x$ , broadening  $g(E_v)$  with always lower  $\Delta G^f$  (Eq. 16).

$$\Delta G^f = \Delta H^f - T\Delta S^f \approx \hat{E}_v - T\Delta S_{O_2} - \frac{\sigma_{E_v}^2}{2RT} \quad (16)$$

Eq. 16 extends to the equilibrium constant  $K_p$  in Eq. 49 suggesting effects from  $\sigma_{E_v}$  could result in quadratic behavior in that extends to the Van't Hoff diagram (Figure 4b). If disordered materials exhibit nonlinear behavior in the Van't Hoff diagram, it could be possible for future studies to fit an estimate of  $\sigma_{E_v}$  experimentally.

$$\ln(K_p) = -\frac{\Delta G^f}{RT} = \frac{\sigma_{E_v}^2}{2R^2T^2} - \frac{\hat{E}_v}{RT} + \frac{\Delta S_{O_2}}{2R} \quad (17)$$

Altogether, Eqs. 13 and 14 for  $\Delta H^f$  and  $\Delta S^f$  correct for the substantial thermodynamic effects of site-differences in a disordered lattice, previously calculated with an MLUIP. By treating vacancy energies as a distribution  $g(E_v)$ , the predicted thermodynamics of LE and HE samples separate in Figure 3d similar to that seen experimentally in Figure 2b with smaller  $\Delta H^f$  and  $\Delta S^f$  values for HE compositions. This agreement suggests a potential narrative, summarized in Figure 3e, for explaining large variations in oxygen vacancy behavior. Mismatches in A-site cation sizes result in straining bonds between oxygen and the B-site cations (Figure 3b). The resulting variance in the vacancy energy (Figure 3c) means a fraction of strained oxygen sites are favorable for vacancies decreasing the effective  $\Delta H^f$  and  $\Delta S^f$ . This could explain why HE materials exhibited more oxygen vacancy growth at low temperature (Figure 1a).

Figure 4 gives a numerical illustration of the implications of including  $\sigma_{E_v}$  with Eqs. 13-14 on the oxygen vacancy model described by Eq. 4. Two types of oxygen vacancies are compared: those with nearly uniform formation energies ( $\sigma_{E_v} = 0.02\text{eV}$ ) as might be seen in binary or LE oxides, and those with broad formation energies ( $\sigma_{E_v} = 0.2\text{eV}$ ) as might be seen in HE samples. Both are centered about  $\hat{E}_v = 1\text{eV}$  (Figure 4a). In Figure 4b-c, it is assumed the oxygen formation entropy minus the vibrational entropy is constant ( $\frac{1}{2}\Delta S_{O_2} - \Delta S_{\text{vib}} = 0.8\text{ eV/K}$ ). The Van't Hoff graph in Figure 4b, calculated from Eq. 49, predicts that a larger  $\sigma_{E_v}$  leads to a flatter  $K_{p,\text{ox}}$ , a prediction in direct agreement with experimental results (Figure 1a). Figure 4c predicts vacancy concentration  $\delta_T$  from Eq. 4 finding that a larger  $\sigma_{E_v}$  results in higher  $\delta_T$  at low temperatures, also consistent with experimental results (Figure 1a). Figure 4d is a sensitivity analysis showing how the statistical effects of  $\sigma_{E_v}$  on  $\Delta G^f$  (the term  $-\sigma_{E_v}^2/2RT$  from Eq. 16) evolves in  $\sigma_{E_v}$ -T space. It is necessary to include the effects of broadened oxygen vacancy energy when this term is non-trivial compared to  $\hat{E}_v$  and  $\Delta S_{O_2}$ , for example, when it

is  $\geq 0.05\text{eV}$  (4.8  $\text{kJ/mol}$ ) which occurs at  $\sigma_{E_v} > 0.1\text{ eV}$  and low temperatures. This effect could be broadly applicable to other defects.

### III. CONCLUSION

Through A-site substitution, high-entropy (HE) perovskites synthesized in this study show substantially different oxygen vacancy formation behavior than low-entropy (LE) samples. In turn, oxygen vacancy formation  $\Delta H^f$  and  $\Delta S^f$  derived from established defect modeling techniques were both lower for HE samples. Variance in the ionic radii across A-site cations ( $\sigma_A$ ) is shown to be a stronger predictor of  $\Delta H^f$  and  $\Delta S^f$  than other compositional descriptors, giving insight into the unique capability of high-entropy A-sites to tune oxygen vacancy formation.

A computational investigation using a machine learning interatomic potential finds that these A-site size variations lead to distortion of the oxygen-B-site bonds which modulate oxygen bonding energy. To consider these sites differences, a statistical approach to estimating  $\Delta H^f$  and  $\Delta S^f$  is employed, showing promising agreement with experimental results. This approach suggests having a fraction of oxygen sites that are strained and prefer vacancy has the dual effect of lowering the effective enthalpy of formation while also decreasing the configurational entropy of oxygen vacancies. Together, these effects result in more vacancies at low temperatures and linear vacancy formation upon increasing temperature. It is proposed that future studies on oxygen vacancies in high-entropy oxides consider the whole distribution of vacancy formation energies  $g(E_v)$  to better account site variations in the high-disordered system. Based on trends observed in his study, the A-site size variance  $\sigma_A$  could be an easily-computed indicator of important statistical phenomena, and thus a critical parameter for the property design of multifunctional high-entropy oxides. Beyond SOECs, oxygen vacancy defects are vital for batteries [31], catalysts [32], integrated circuits [33], and gas sensors [34].

### IV. METHODS

#### A. Composition Descriptor Calculations

Materials reported are chosen to span low and high entropy variations of the common SOEC material LSCF (LE-1 in Table I). All have the same B-site,  $(\text{Co}_{0.2}\text{Fe}_{0.8})$ , as LSCF. The B-site's Co-Fe ratio is known to govern electrical conductivity and thermal expansion and the chosen composition has been refined in the SOEC literature to strike a balance between the two properties [19]. Of 14 compositions chosen, 3x have low-entropy (LE) A-sites (2-3 cation elements) and 11x samples have high-entropy (HE) A-sites ( $\geq 5$  cation elements). Some A-site elements were chosen randomly as equimolar combinations of Lanthanides and Alkaline Earth (AE) metals, while others were chosen to span a set of common compositional parameters describing the set of cations in the A-site (Table

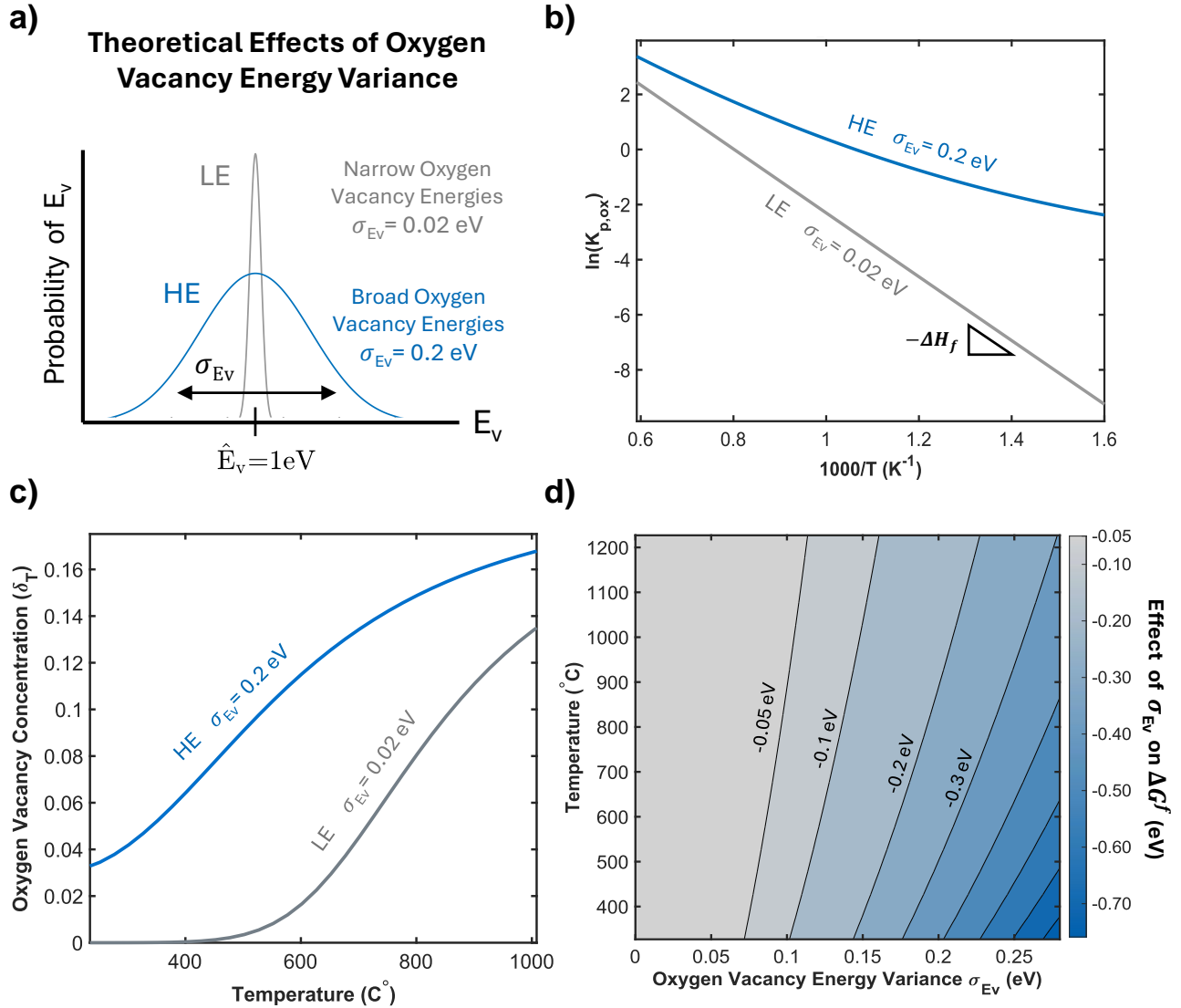


FIG. 4. a) Theoretical oxides with low (LE) and high (HE) oxygen vacancy energy variance  $\sigma_{Ev}$  and equal  $\hat{E}_v$  b) Van't Hoff diagram for defined LE and HE oxides using Eqs. 13-14 c) simulated  $\delta_T$  as a function of temperature d) the sensitivity of  $\Delta G_f$  to vacancy energy broadening as a function of  $\sigma_{Ev}$  and temperature

I). We selected several parameters to quantitatively describe the characteristics of the A sites. The first parameter is the A-site molar fraction of divalent AE metals (Ca, Sr, or Ba)  $X_{2+}$  (Eq.18) which is known to shift the charge balance relative to other trivalent (3+ oxidation) Lanthanide A-site cations.

$$X_{2+} = X_{Ca} + X_{Sr} + X_{Ba} \quad (18)$$

The Goldschmidt tolerance factor  $t$  (Eq.19) [35] relates to the average A-site cation ionic radius ( $\hat{r}$ ) while A-site size variance  $\sigma_A$  (Eq.1 earlier in text) describes the variance among  $N$  different A-site cation radii ( $r_i$ ) respectively.

$$t = \frac{\hat{r}_A + r_O}{\sqrt{2}(\hat{r}_B + r_O)} \quad (19)$$

The last parameter,  $\Delta S_{mix}$ , is the A-site entropy of mixing  $N$  elements with mole fractions  $X_i$  and is larger for more elements

mixed. Table I lists 14 materials than span a wide range of  $X_{2+}$ ,  $t$ ,  $\sigma_A$ , and  $\Delta S_{mix}$  to clarify which parameters strongly affect the formation of oxygen vacancies.

$$\Delta S_{mix} = -R \sum_i^N X_i \ln X_i \quad (20)$$

To calculate tolerance factors  $t$  (Eq. 19) and size variances  $\sigma_A$  (Eq. 1), Shannon ionic radii values are used [36]. It is assumed the coordination number of oxygen is two, B-sites is 6, and A-sites is 12. While the oxidation and spin states of iron and cobalt can be subject to change depending on the environment, it is assumed most iron and cobalt are in the 3+ oxidation state. Finally, we adopt assumptions about the spin states previously used for a similar material with iron in a high spin state and cobalt in an intermediate spin state taken as the average of the high and low spin state ionic radii [37].

## B. Material Synthesis

The solution combustion synthesis begins with stoichiometric mixing of metal nitrate precursors from Thermo Fisher Scientific: La(NO<sub>3</sub>)<sub>3</sub> (99.9%), Sr(NO<sub>3</sub>)<sub>2</sub> (≥99%), Ca(NO<sub>3</sub>)<sub>2</sub> (≥99%), Ba(NO<sub>3</sub>)<sub>2</sub> (≥99%), Nd(NO<sub>3</sub>)<sub>3</sub>·6(H<sub>2</sub>O) (99.9%), Sm(NO<sub>3</sub>)<sub>3</sub>·6(H<sub>2</sub>O) (99.9%), Gd(NO<sub>3</sub>)<sub>3</sub>·6(H<sub>2</sub>O) (99.9%), Y(NO<sub>3</sub>)<sub>3</sub>·6(H<sub>2</sub>O) (99.9%), Fe(NO<sub>3</sub>)<sub>2</sub>·9(H<sub>2</sub>O) (≥98%), and Co(NO<sub>3</sub>)<sub>2</sub>·6(H<sub>2</sub>O) (≥98%). Precursors were dissolved in 100mL of deionized water to form a 1M solution of precursor cations in a 500mL Pyrex beaker. Sucrose (Sigma-Aldrich Omnipur) is added as a fuel in a fuel-oxidizer ratio of 1.0 (1M sucrose). The solution is stirred with a magnetic stir rod and dehydrated at 50°C on a hot plate for ~12 hours or until solution forms a gel. The rod is removed and temperature raised to 350°C to initiate the combustion reaction. When the gel had fully burned, about 30 minutes, the product is removed and ground with a mortar and pestle. The powders then are placed in an alumina crucible and annealed at 800°C for 90 minutes with a 4°C/min ramp rate. Powders collected from the solution combustion synthesis were processed with high-energy ball-milling. Oxide powders (~10g) were dissolved in 30mL of hexane (99.9% Fischer Chemical) and placed in a 50mL stainless steel vial in a Retsch Cryomill. The powder underwent 3 hours of room-temperature wet-milling at 30Hz. Powders were collected after drying the resulting slurry on a 50°C hot plate.

## C. Characterization Experiments

The crystal structure (see Figure S1) of the synthesized samples was investigated by X-ray diffraction (XRD, PANalytical Empyrean) with a Cu source (K $\alpha$ , 1.54 Å of the wavelength). The morphologies of synthesized powders were examined using scanning electron microscopy (SEM) on an FEI Magellan 400 XHR, operating at an accelerating voltage of 5 kV and a beam current of 25 pA. SEM/EDS was conducted using the same instrument with an accelerating voltage of 20 kV and a beam current of 3.2 nA.

TGA is a common approach to measuring oxygen vacancies [4, 10–12, 14] and was found to be in agreement with iodometric titration and columbic titration methods [17]. The TGA proto-

col starts with a 1.5 hour 900°C preheating step to ensure mass stability. The 50-70mg samples are cooled and reheated with 1-2 hour holds every 100°C from 500°C to 1000°C in a Setaram LABSYS evo TGA-DSC (see Figure S2). Experiments were performed in air ( $pO_2=0.21$  atm) to be consistent with high  $pO_2$  present for SOEC air electrode. TGA mass changes at each temperature  $\Delta m_T$  (mg) relative to the initial mass  $m_0$  (mg) were used to calculate the oxygen non-stoichiometry changes  $\Delta\delta_T$  for a material with a theoretical molar mass  $M_w$  with Eq. 21.

$$\Delta\delta_T = \frac{\Delta m_T}{m_0} \frac{M_w}{16} \quad (21)$$

## D. Atomistic Simulations

In this paper, the Matlantis PFP estimator, trained on data without the Hubbard U correction, is used to perform structural relaxation using the LBFGS algorithm. We conducted atomistic simulations using an MLUIP provided by Matlantis [38]. Its stated mean average error of 0.03 eV for disordered systems is small compared to calculated vacancy formation energy values in the range of 0.15–1.4 eV [25]. The structural analysis determined B-site bonding to oxygen with 1.1 Å radius collision spheres. For vacancy formation energy, the program iterates over removing 768 oxygen sites in a 1280 atom supercell (Fig S3) randomly populated with cations in stoichiometric ratios with no initial oxygen vacancies.

## V. DATA AND CODE AVAILABILITY

The data and code that support the findings of this study are available from the corresponding authors upon reasonable request.

## ACKNOWLEDGMENT

The authors gratefully acknowledge the financial and technical support provided by Genvia and the Commissariat à l’Énergie Atomique et aux Énergies Alternatives (CEA), France.

---

[1] E. Y. Pikalova, E. G. Kalinina, N. S. Pikalova, and E. A. Filonova, *Materials* **15**, 8783 (2022), number: 24 Publisher: Multidisciplinary Digital Publishing Institute.

[2] H. Xiang, Y. Xing, F.-z. Dai, H. Wang, L. Su, L. Miao, G. Zhang, Y. Wang, X. Qi, L. Yao, H. Wang, B. Zhao, J. Li, and Y. Zhou, *Journal of Advanced Ceramics* **10**, 385 (2021).

[3] H. Bae, I.-H. Kim, B. Singh, A. Bhardwaj, and S.-J. Song, *Solid State Ionics* **347**, 115251 (2020).

[4] M.-B. Choi, S.-Y. Jeon, H.-N. Im, and S.-J. Song, *Journal of Alloys and Compounds* **513**, 487 (2012).

[5] C. M. Rost, E. Sachet, T. Borman, A. Moballegh, E. C. Dickey, D. Hou, J. L. Jones, S. Curtarolo, and J.-P. Maria, *Nature Communications* **6**, 8485 (2015), publisher: Nature Publishing Group.

[6] L. Su, H. Huyan, A. Sarkar, W. Gao, X. Yan, C. Addiego, R. Kruk, H. Hahn, and X. Pan, *Nature Communications* **13**, 2358 (2022).

[7] B. Xu, J. Park, D. Zhang, H. A. De Santiago, W. Li, X. Liu, J. Luo, S. Lany, and Y. Qi, *Chemistry of Materials* **36**, 4990 (2024), publisher: American Chemical Society.

[8] M. Zhang, X. Duan, Y. Gao, S. Zhang, X. Lu, K. Luo, J. Ye, X. Wang, Q. Niu, P. Zhang, and S. Dai, *ACS Applied Materials & Interfaces* **15**, 45774 (2023), publisher: American Chemical Society.

[9] M.-B. Choi, D.-K. Lim, E. Wachsman, and S.-J. Song, *Solid State Ionics* **221**, 22 (2012).

[10] M. Oishi, K. Yashiro, K. Sato, J. Mizusaki, and T. Kawada, *Journal of Solid State Chemistry* **181**, 3177 (2008).

[11] H. Luo, Y. Shin, Y. Yu, D. Cetin, K. Ludwig, U. Pal, S. N. Basu, S. Gopalan, and X. Lin, *Applied Surface Science* **323**, 65 (2014).

[12] H. Bae, J. Hong, B. Singh, A. K. Srivastava, J. H. Joo, and S.-J. Song, *Journal of The Electrochemical Society* **166**, F180 (2019).

[13] J. Park, B. Xu, J. Pan, D. Zhang, S. Lany, X. Liu, J. Luo, and Y. Qi, *npj Computational Materials* **9**, 29 (2023).

[14] J. Mizusaki, M. Yoshihiro, S. Yamauchi, and K. Fueki, *Journal of Solid State Chemistry* **58**, 257 (1985).

[15] S.-Y. Jeon, M.-B. Choi, J.-H. Hwang, E. D. Wachsman, and S.-J. Song, *Journal of Solid State Electrochemistry* **16**, 785 (2012).

[16] M.-B. Choi, S.-Y. Jeon, B. Singh, Y.-S. Yoo, J.-H. Hwang, and S.-J. Song, *Acta Materialia* **65**, 373 (2014).

[17] M. Karppinen, M. Matvejeff, K. Salomäki, and H. Yamamichi, *Journal of Materials Chemistry* **12**, 1761 (2002).

[18] A. M. Deml, A. M. Holder, R. P. O’Hayre, C. B. Musgrave, and V. Stevanović, *The Journal of Physical Chemistry Letters* **6**, 1948 (2015).

[19] S. P. Jiang, *International Journal of Hydrogen Energy* **44**, 7448 (2019).

[20] M. Kuhn, S. Hashimoto, K. Sato, K. Yashiro, and J. Mizusaki, *Solid State Ionics* **195**, 7 (2011).

[21] M. Søgaard, P. Vang Hendriksen, and M. Mogensen, *Journal of Solid State Chemistry* **180**, 1489 (2007).

[22] E. B. Starikov and B. Nordén, *The Journal of Physical Chemistry B* **111**, 14431 (2007), publisher: American Chemical Society.

[23] A. Cornish-Bowden, *Encyclopedia of Biophysics*, edited by G. Roberts and A. Watts (Springer, 2018) pp. 1–6.

[24] A. Pan, T. Kar, A. K. Rakshit, and S. P. Moulik, *The Journal of Physical Chemistry B* **120**, 10531 (2016), publisher: American Chemical Society.

[25] S. Takamoto, C. Shinagawa, D. Motoki, K. Nakago, W. Li, I. Kurata, T. Watanabe, Y. Yayama, H. Iriguchi, Y. Asano, T. Onodera, T. Ishii, T. Kudo, H. Ono, R. Sawada, R. Ishitani, M. Ong, T. Yamaguchi, T. Kataoka, A. Hayashi, N. Charoenphakdee, and T. Ibuka, *Nature Communications* **13**, 2991 (2022).

[26] A. H. Larsen, J. J. Mortensen, J. Blomqvist, I. E. Castelli, R. Christensen, M. Dulak, J. Friis, M. N. Groves, B. Hammer, C. Hargas, E. D. Hermes, P. C. Jennings, P. B. Jensen, J. Kermode, J. R. Kitchin, E. L. Kolsbjer, J. Kubal, K. Kaasbjer, S. Lysgaard, J. B. Maronsson, T. Maxson, T. Olsen, L. Pastewka, A. Petersen, C. Rostgaard, J. Schiøtz, O. Schütt, M. Strange, K. S. Thygesen, T. Vegge, L. Vilhelmsen, M. Walter, Z. Zeng, and K. W. Jacobsen, *Journal of Physics: Condensed Matter* **29**, 273002 (2017), publisher: IOP Publishing.

[27] Y. Jing and N. Aluru, *Journal of Power Sources* **445**, 227327 (2020).

[28] V. Stevanović, S. Lany, X. Zhang, and A. Zunger, *Physical Review B* **85**, 115104 (2012).

[29] E. N. Rudisill and M. D. LeVan, *Chemical Engineering Science* **47**, 1239 (1992).

[30] O. Elmutasim, A. G. Hussien, A. Sharan, S. AlKhoori, M. A. Vasiliades, I. M. A. Taha, S. Kim, M. Harfouche, A.-H. Emwas, D. H. Anjum, A. M. Efstathiou, C. T. Yavuz, N. Singh, and K. Polychronopoulou, *ACS Applied Materials & Interfaces* **16**, 23038 (2024), publisher: American Chemical Society.

[31] Z.-K. Tang, Y.-F. Xue, G. Teobaldi, and L.-M. Liu, *Nanoscale Horizons* **5**, 1453 (2020), publisher: The Royal Society of Chemistry.

[32] K. Zhu, F. Shi, X. Zhu, and W. Yang, *Nano Energy* **73**, 104761 (2020).

[33] J. Lee, W. Schell, X. Zhu, E. Kioupakis, and W. D. Lu, *ACS Applied Materials & Interfaces* **11**, 11579 (2019), publisher: American Chemical Society.

[34] M. Al-Hashem, S. Akbar, and P. Morris, *Sensors and Actuators B: Chemical* **301**, 126845 (2019).

[35] V. M. Goldschmidt, *Naturwissenschaften* **14**, 477 (1926).

[36] R. D. Shannon, *Acta Crystallographica Section A: Crystal Physics, Diffraction, Theoretical and General Crystallography* **32**, 751 (1976), publisher: International Union of Crystallography.

[37] S. Gangopadhyay, A. E. Masunov, T. Inerbaev, J. Mesit, R. K. Guha, A. K. Sleiti, and J. S. Kapat, *Solid State Ionics* **181**, 1067 (2010).

[38] “Matlantis, software as a service style material discovery tool,” <https://matlantis.com/> (2024).

**SUPPLEMENTAL INFORMATION: A STATISTICAL UNDERSTANDING OF OXYGEN VACANCIES IN DISTORTED HIGH-ENTROPY OXIDES**

**I. MATERIAL CHARACTERIZATION**

The distribution of elements in oxide powders were investigated with scanning electron microscopy (SEM) paired with energy dispersive X-ray (EDX) analysis for sample HE-2 (Figure S1a) illustrating the homogeneous distributions of 7 cations in both A- and B-sites. X-ray diffraction (XRD) results in Figure 1b shows comparable diffraction data across all 14 samples suggesting synthesized samples are of the same perovskite phase (orthorhombic *Pnma*). While peak positions and profiles are similar, small positional differences (ex. LE-1 shifted left) can be explained by variations in lattice parameters. This can be due to the B-site cation being larger or smaller depending on their oxidation state. Different molar fractions of A-site 2+ cations ( $X_{2+}$ ) and other factors can result in smaller 4+ oxidized iron or cobalt to maintain charge neutrality.

Thermogravimetric characterization of oxygen vacancy formation (Figure S2) followed stepwise heating with corresponding decreases in mass for oxygen loss. The mass is found to stabilize within minutes suggesting fast dynamics of oxygen vacancy formation resulting in an equilibrium. A blank crucible run was subtracted from all data to remove the contributions from the alumina crucible.

**II. ATOMISTIC SIMULATION SUPERCELLS**

Simulation structures use a simple perovskite cell found to match XRD data well to form a 4x4x4 supercell (Figure S3) with 1280 atoms (768 oxygen sites). Sites are then randomly populated (no local ordering) with elements in equal ratios to the desired composition (no vacancies). The structure is then relaxed to minimize the energy by perturbing site positions and cell volumes.

**III. EFFECTS OF ENERGY PERTURBATIONS ON VACANCY THERMODYNAMICS**

Unlike binary oxides, disordered oxides have heterogeneous oxygen sites with a distribution of different binding energies. These perturbations in binding energy can affect the bulk thermodynamics of forming oxygen vacancies, and consequently, the equilibrium vacancy concentrations at different temperatures and pressures. The objective of this section is to derive a first-order approximation of the effects of vacancy energy variance ( $\sigma_\epsilon$ ) on the bulk thermodynamic properties. First, we find expressions for the vacancy chemical potential ( $\mu_v$ ), enthalpy ( $h_v$ ), and entropy ( $s_v$ ) as a function of binding energy variance. Then, we compare  $\mu_v$  with the typical

expression for vacancy activity to find the influence of  $\sigma_\epsilon$  on the oxygen vacancy formation reaction's standard enthalpy  $\Delta H^f$  and entropy  $\Delta S^f$ . The result is an intuitive relation for how tuning  $\sigma_\epsilon$  (or similarly  $\sigma_{Ev}$ ) through lattice distortion can shift the oxygen vacancy equilibrium.

**A. Problem Setup and Vacancy Chemical Potential**

Consider a system of  $n$  vacancies spread over  $N$  oxygen sites so the fraction of vacant sites can be given by  $x = n_v/N = \delta_T/3$ . Each site has a unique vacancy free energy  $\epsilon_i$  ( $i=1,2,\dots,N$ ) centered about an average  $\hat{\epsilon}$  (Eq. 22) with variance  $\sigma_\epsilon$  (Eq. 23). Vacancy free energy can be thought of as the opposite of oxygen binding free energy. The deviation of  $\epsilon_i$  from the mean can be defined as  $\delta_i = \epsilon_i - \hat{\epsilon}$ . Note that  $\delta_i$  is deviation in free energy, not the vacancy concentration  $\delta_T$ , and that  $\epsilon$  represents the free energy of an oxygen on a lattice site and includes binding energy and vibrational (phonon) entropy.

$$\hat{\epsilon} = \frac{1}{N} \sum_{i=1}^N \epsilon_i \quad (22)$$

$$\sigma_\epsilon = \frac{1}{N} \sum_{i=1}^N (\epsilon_i - \hat{\epsilon})^2 = \frac{1}{N} \sum_{i=1}^N \delta_i^2 \quad (23)$$

We can relate the chemical potential of a vacancy  $\mu_v$  to the probability of site occupancy in an open system with the grand canonical ensemble. Since each site can bind to a maximum of one atom, the particle acts like an ideal Fermion and the expected number of vacancies on site  $i$ ,  $N_i$ , can be given by the Fermi distribution (Eq. 24) where  $\beta = 1/k_B T$ ,  $k_B$  is the Boltzmann constant, and  $T$  is temperature. This is intuitive because if an oxygen atom is indifferent to bonding to the site ( $\epsilon_i = \mu_v$ ) then the probability of vacancy is 1/2.

$$N_i = \frac{1}{1 + e^{(\epsilon_i - \mu_v)\beta}} \quad (24)$$

The site vacancy fraction  $x$  can be rewritten by noting that the number of vacancies  $n_v$  is given by the average vacancy probability  $N_i$  over all sites (Eq. 25). Each site's free energy  $\epsilon_i$  can be written in terms of  $\hat{\epsilon}$ , a constant, and  $\delta_i$ .

$$x = \frac{n_v}{N} = \frac{\sum_{i=1}^N N_i}{N} = \frac{1}{N} \sum_{i=1}^N \frac{1}{1 + e^{(\hat{\epsilon} - \mu_v)\beta} e^{\delta_i \beta}} \quad (25)$$

Inverting this expression can yield the chemical potential  $\mu_v$  as a function of site vacancy, but in practice it cannot be done analytically. The corresponding chemical potential of oxygen is the the opposite of that for a vacancy ( $\mu_O = -\mu_v$ ).

In the case of a small deviation  $\delta_i$ , the right side of Eq. 25 can be Taylor expanded to the second order with

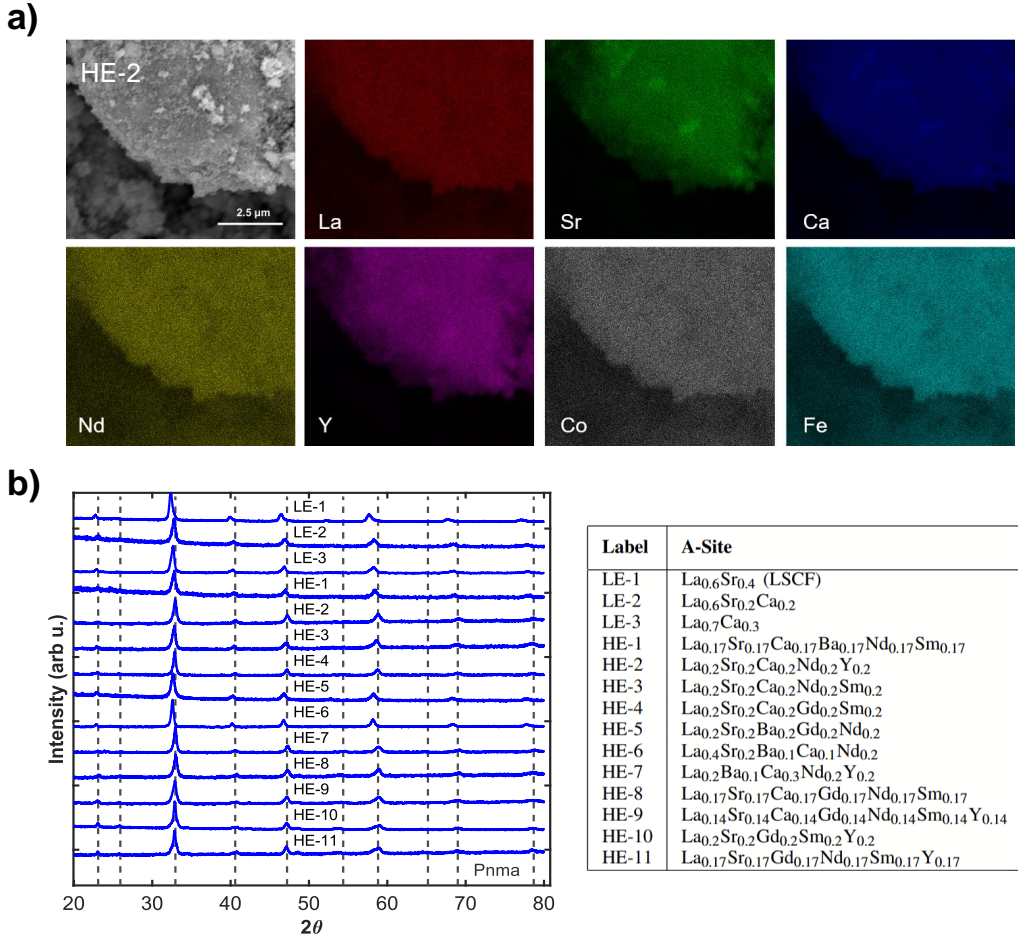


Fig. S 1. (a) SEM-EDS images of HE-2 shows that all cations in a high-entropy sample are evenly distributed at the micro-scale. (b) XRD spectra at room temperature for all synthesized samples suggests equivalent structures.

respect to  $\delta_i$ , truncating higher order terms. This approximation yields Eq. 26 expanding about  $\delta_0 = 0$  where we define  $z := e^{(\hat{\epsilon} - \mu_v)\beta}$  for brevity. The first order terms with respect to  $\delta_i$  sum to zero over all sites as per the definition of  $\hat{\epsilon}$  (Eq. 22). The summation over the second order terms results in the definition of  $\sigma_\epsilon$  (Eq. 23) giving a simplified expression for site vacancy  $x$  as a function of  $z$  and  $\sigma_\epsilon$ .

$$x \approx \frac{1}{N} \sum_{i=1}^N \left[ \frac{1}{1+z} - \frac{z}{(1+z)^2} \beta \delta_i + \frac{z^2 - z}{2(1+z)^3} \beta^2 \delta_i^2 \right] \\ = \frac{1}{1+z} + \frac{z^2 - z}{2(1+z)^3} \beta^2 \sigma_\epsilon^2 \quad (26)$$

For a simplified system with homogeneous oxygen sites, the energy variance  $\sigma_\epsilon = 0$  leading to a recognizable expression for vacancy chemical potential  $\mu_v$  (Eq. 27). We find  $z$  this for this case,  $z_0 := \frac{1-x}{x}$ , and solve for  $\mu_v$ . The second term on the right is the standard adsorption isotherm, the log of the vacancy fraction over the occu-

pied site fraction.

$$\mu_v = \hat{\epsilon} + k_B T \ln\left(\frac{x}{1-x}\right) \quad (27)$$

However, when  $\sigma_\epsilon \neq 0$  the expression for  $\mu_v$  becomes more complex. Given only a small dispersion  $\sigma_\epsilon^2$  is of interest, a compact solution can be found by imposing the form  $z = z_0(1+z_1)$  where  $z_1$  is of the order  $\beta^2 \sigma_\epsilon^2$ . Then the vacancy fraction is given by Eq. 28. The second term is replaced by  $z_0$  since we are focusing on the leading order term.

$$x = \frac{1}{1+z_0} - \frac{z_0}{(1+z_0)^2} z_1 + \frac{z_0^2 - z_0}{2(1+z_0)^3} \beta^2 \sigma_\epsilon^2 \quad (28)$$

Noticing that  $\frac{1}{1+z_0} = x$  the remaining coefficients can be matching resulting in an expression for  $z_1$  (Eq. 29). In the last term,  $z$  is replaced with  $z_0$  as we are focused on the leading term.

$$z_1 = \frac{z_0 - 1}{2(1+z_0)} \beta^2 \sigma_\epsilon^2 = \left(\frac{1}{2} - x\right) \beta^2 \sigma_\epsilon^2 \quad (29)$$

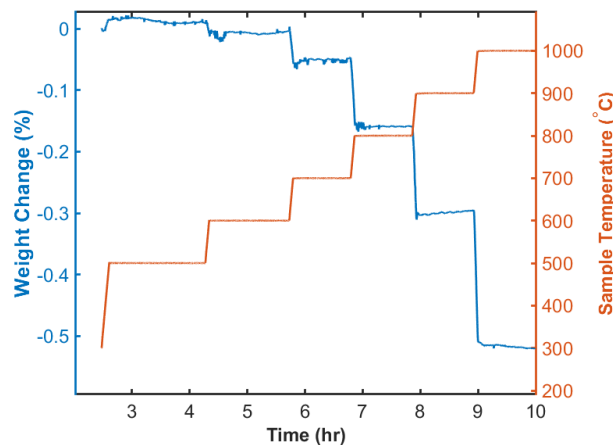


Fig. S 2. TGA temperature profile (orange) and resulting mass change (blue) from oxygen vacancy formation in LE-1. A blank crucible run as been subtracted from results.

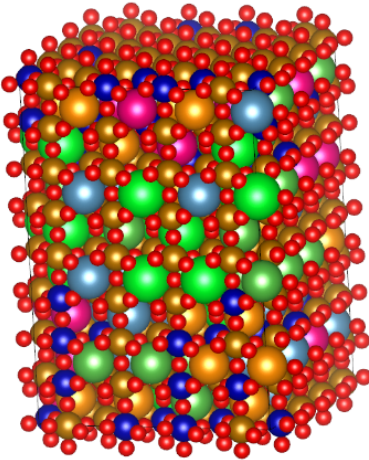


Fig. S 3. A generated supercell of 1280 atoms for HE-3: O is red, Fe is brown, Co is blue, La is dark green, Sr is light green, Sm is pink, Ca is light blue, and Nd is orange.

Substituting in values for  $z_0$  and  $z_1$  we arrive at an expression (Eq. 30) for  $z$  as a function of  $x$  and  $\sigma_\epsilon$ , an inversion of the earlier Eq. 26.

$$z = e^{(\hat{\epsilon} - \mu_v)\beta} = \frac{x}{1-x}(1 + (x - \frac{1}{2})\beta^2\sigma_\epsilon^2) \quad (30)$$

This first-order inversion allows us to resolve the effects of  $\sigma_\epsilon$  on the vacancy chemical potential  $\mu_v$  with Eq. 31.

$$\mu_v = \hat{\epsilon} + k_B T [\ln(\frac{x}{1-x}) + \ln(1 + (x - \frac{1}{2})\beta^2\sigma_\epsilon^2)] \quad (31)$$

We can make the approximation  $\ln(1+x) \approx x$  for small values of  $x$  resulting in a clean expression for vacancy chemical potential that includes the first order effects of

energy variance  $\sigma_\epsilon$  (Eq. 32).

$$\mu_v = \hat{\epsilon} + k_B T [\ln(\frac{x}{1-x}) + (x - \frac{1}{2})\frac{\sigma_\epsilon^2}{(k_B T)^2}] \quad (32)$$

The above result is appealing in that it connects transparently the activity correction coefficient  $\gamma$  with the degree of free energy dispersion via the term  $(x - 1/2)\beta^2\sigma_\epsilon^2$  so we can say  $\gamma = 1 + (x - 1/2)\beta^2\sigma_\epsilon^2$ . We can also see that at small vacancy fractions (small  $x$ ) energy variance  $\sigma_\epsilon$  reduces the vacancy chemical potential.

### B. Deriving the Equilibrium Constant to Find $\Delta H^f$ and $\Delta S^f$

To form an oxygen vacancy, gaseous oxygen is released into the environment as per the reaction in Eq. 33. This formation reaction is in equilibrium, so the chemical potential of the lattice oxygen (the opposite of vacancy chemical potential) equals the half the chemical potential of gaseous oxygen (Eq. 34). Here, we ignore the contribution of charge compensation (coupling to electron holes) described in the main text, but the reaction is easily translated by including hole concentration in the law of mass action.



$$\frac{1}{2}\mu_{O_2} = -\mu_v \quad (34)$$

The average free energy per vacancy  $\hat{\epsilon}$  can be considered in terms of the average internal energy of a vacancy  $\hat{u}_v$  and the oxygen vibrational entropy  $S_O^{vib}$  in Eq. 35. The vacancy enthalpy,  $\hat{h}_v$ , should be comparable to  $\hat{u}_v$  in incompressible solids and can be interpreted as the opposite of oxygen bonding enthalpy. We assume that the entropy component of  $\hat{\epsilon}$  is the opposite of the oxygen atom vibrational entropy ( $S_O^{vib}$ ), assumed to be approximately constant across sites.

$$\mu_v = (\hat{h}_v + TS_O^{vib}) + k_B T \ln(\frac{x}{1-x}) + (x - \frac{1}{2})\frac{\sigma_\epsilon^2}{k_B T} \quad (35)$$

On the other side of Eq. 34, the gaseous oxygen chemical potential ( $\mu_{O_2}$ ) can be found from tabulated values. The reference enthalpy  $H_{O_2}^0$  includes the formation energy of the  $O_2$  from monotonic oxygen. The oxygen's reference entropy  $S_{O_2}^0$  is large due to the large number of accessible states to an unbound gas molecule. The final term in Eq. 36 is the ideal mixing pressure correction where  $P_{O_2}$  is the partial pressure of oxygen and  $P_{O_2}^0 = 0.1$  MPa is the reference pressure for  $S_{O_2}^0$ .

$$\mu_{O_2} = H_{O_2}^0 - TS_{O_2}^0 + k_B T \ln(\frac{P_{O_2}}{P_{O_2}^0}) \quad (36)$$

When the two chemical potentials are equated as per Eq. 34 and like terms grouped, we arrive at Eq. 37.

$$\begin{aligned} -(\hat{h}_v + \frac{1}{2}H_{O_2}^0) + T(\frac{1}{2}S_{O_2}^0 - S_O^{\text{vib}}) - (x - \frac{1}{2})\frac{\sigma_\epsilon^2}{k_B T} \\ = \frac{1}{2}k_B T \ln(\frac{P_{O_2}}{P_{O_2}^0}) + k_B T \ln(\frac{x}{1-x}) \quad (37) \end{aligned}$$

By assembling the terms including vacancy fraction  $x$  in the above expression, we can extract the log of the equilibrium constant  $K_{p,\text{ox}}$  for vacancy formation.  $K_{p,\text{ox}}$  is defined for the vacancy formation reaction (Eq. 33) in Eq. 38 as the vacancy site fraction over the oxygen occupancy site fraction with a term for oxygen partial pressure. The Gibbs of formation for the vacancy formation  $\Delta G^f$  is defined by its relation to the equilibrium constant (Eq. 38).

$$\ln[\frac{x}{1-x}(\frac{P_{O_2}}{P_{O_2}^0})^{1/2}] := \ln(K_{p,\text{ox}}) = -\frac{\Delta G^f}{k_B T} \quad (38)$$

By collecting terms from Eq. 37 to form Eq. 38, we find a final expression for Gibb's of formation  $\Delta G^f$  (Eq. 39) as a function of constitutive thermodynamic values for environmental oxygen ( $H_{O_2}^0, S_{O_2}^0$ ) and lattice oxygen ( $\hat{h}_v, S_O^{\text{vib}}, \sigma_\epsilon$ ).

$$\Delta G^f = (\hat{h}_v + \frac{1}{2}H_{O_2}^0) - T(\frac{1}{2}S_{O_2}^0 - S_O^{\text{vib}}) + (x - \frac{1}{2})\frac{\sigma_\epsilon^2}{k_B T} \quad (39)$$

Note that the standard adsorption isotherm term,  $\ln(\frac{x}{1-x})$ , has disappeared in Eq. 39 because it was used to form the equilibrium constant  $K_{p,\text{ox}}$ . The effects of vacancy energy dispersion ( $\sigma_\epsilon$ ) have carried over to lower the value of  $\Delta G^f$  when  $x < 1/2$ , making the formation of vacancies more favorable. In this final step, we find  $\Delta H^f$  and  $\Delta S^f$  from  $\Delta G^f$ . An expression for  $\Delta H^f$  can be found from its definition (Eq. 40) resulting in Eq. 41.

$$\Delta H^f := \frac{\delta(\beta\Delta G^f)}{\delta\beta}, \quad \beta = \frac{1}{k_B T} \quad (40)$$

$$\Delta H^f = \hat{h}_v + \frac{1}{2}H_{O_2}^0 - \frac{(1-2x)\sigma_\epsilon^2}{k_B T} \quad (41)$$

It can be seen that introducing energy dispersion with  $\sigma_\epsilon$  lowers the effective  $\Delta H^f$  when  $x$  is small. This is because a small number of vacancies will thermodynamically prefer to form on sites with lower than average ( $\hat{h}_v$ ) enthalpy. Because low-energy sites are weighted higher, the statistical average of vacancy formation enthalpy is lowered.

In order to use Eq. 41 in computational predictions, we assume that oxygen enthalpy  $H_{O_2}^0$  is a constant  $O_2$  formation energy  $E_{O_2}$  and vacancy enthalpy  $h_v$  is the difference in lattice energy before ( $E_{\text{bulk}}$ ) and after ( $E_{\text{defect}}$ ) forming a vacancy. This means we can write the vacancy energy  $E_v$  as Eq. 42.

$$E_v := E_{\text{defect}} - E_{\text{bulk}} + \frac{1}{2}E_{O_2} \approx h_v + \frac{1}{2}H_{O_2}^0 \quad (42)$$

When we assume vibrational entropy  $S_O^{\text{vib}}$  is approximately constant across sites, we can attribute any variance in free energy ( $\epsilon$ ) to variance in the vacancy energy  $E_v$  given by Eq. 43.

$$\sigma_\epsilon^2 = \text{Var}(\epsilon) = \text{Var}(E_v) = \sigma_{E_v}^2 \quad (43)$$

This leads to an expression for  $\Delta H^f$  simply as a function of the mean and variance of  $E_v$  over all oxygen sites (Eq. 44).

$$\Delta H^f = \hat{E}_v - \frac{(1-2x)\sigma_{E_v}^2}{k_B T} \quad (44)$$

In the limit  $x \rightarrow 0$  for small vacancy fractions, which is valid since the maximum measured  $x$  in HEPOs is  $x=0.045$ , Eq. 44 simplifies to Eq. 45. Importantly,  $\Delta H^f$  in this form can be directly calculated by sampling  $E_v$  in atomistic simulations.

$$\Delta H^f = \hat{E}_v - \frac{\sigma_{E_v}^2}{k_B T} \quad (45)$$

Next, we can find the formation entropy  $\Delta S^f$  from its definition (Eq. 46) resulting in the final Eq. 47.

$$\Delta S^f := -\frac{\delta\Delta G^f}{\delta T} \quad (46)$$

$$\Delta S^f = \frac{1}{2}S_{O_2}^0 - S_O^{\text{vib}} - \frac{(1-2x)\sigma_{E_v}^2}{2k_B T^2} \quad (47)$$

In the limit  $x \rightarrow 0$ , Eq. 47 turns into the final Eq. 48.

$$\Delta S^f = \frac{1}{2}S_{O_2}^0 - S_O^{\text{vib}} - \frac{\sigma_{E_v}^2}{2k_B T^2} \quad (48)$$

The oxygen reference entropy  $S_{O_2}^0$  is a tabulated value and we can assume  $S_O^{\text{vib}}$  is negligible or a constant offset to  $\Delta S^f$ . This leaves  $\sigma_{E_v}$  as a prominent source of variance in  $\Delta S^f$  between materials. Similar to  $\Delta H^f$ , energy dispersion lowers the value of  $\Delta S^f$ . This is because introducing lower energy oxygen sites increases the probability of those sites being vacant. Having preferred sites for vacancy reduces the configurational entropy from forming a new vacancy, resulting in a lower  $\Delta S^f$ .

This concludes the derivation of the first order effects of  $\sigma_{E_v}$  on  $\Delta H^f$  (Eq. 45) and  $\Delta S^f$  (Eq. 48). Given in these forms,  $\Delta H^f$  and  $\Delta S^f$  can be easily calculated from atomistic simulations. These approximations should be valid in the limit of small energy dispersion  $\sigma_{E_v}$  and small vacancy fraction  $x$ . It can be noted that in Eqs. 39, 45, 48 the identity  $\Delta G^f = \Delta H^f - T\Delta S^f$  holds true. The implications of simplified Eqs. 45 and 48 are given in Figure 4 of the main text.

As a consequence of accounting for energy dispersion, the Van't Hoff plot (log of  $K_{p,\text{ox}}$ ) may be slightly quadratic, as given in Eq. 49. This implies it could be possible in the future to extract an estimate of  $\sigma_{E_v}$  from

careful experiments, giving valuable insight into defect thermodynamics in disordered materials.

$$\ln(K_p) = -\frac{\Delta G^f}{RT} = \left(\frac{\sigma_{\text{Ev}}^2}{2R^2}\right) \frac{1}{T^2} + \left(-\frac{\hat{E}_{\text{v}}}{R}\right) \frac{1}{T} + \left(\frac{\frac{1}{2}\Delta S_{O_2}}{R}\right) \quad (49)$$